

Research Article

Numerical Study on Combustion and Atomization Characteristics of Coaxial Injectors for LOX/Methane Engine

Jiabao Xu ^{1,2}, Ping Jin ^{1,2}, Ruizhi Li,^{1,2} Jue Wang,³ and Guobiao Cai^{1,2}

¹School of Astronautics, Beihang University, Beijing 100191, China

²Key Laboratory of Spacecraft Design Optimization and Dynamic Simulation Technologies, Ministry of Education, China

³System Engineering Division, China Academy of Launch Vehicle Technology, Beijing 100076, China

Correspondence should be addressed to Ping Jin; jinping@buaa.edu.cn

Received 12 January 2021; Revised 13 April 2021; Accepted 22 April 2021; Published 24 May 2021

Academic Editor: Juan Du

Copyright © 2021 Jiabao Xu et al. This is an open access article distributed under the Creative Commons Attribution License, which permits unrestricted use, distribution, and reproduction in any medium, provided the original work is properly cited.

The LOX/methane engine has an admirable performance under a supercritical state. However, the properties of methane change drastically with varying injection temperature. Because the injector can greatly affect the atomization and combustion, this study performed a three-dimensional numerical simulation of atomization, combustion, and heat transfer in a subscale LOX/methane engine to evaluate the effect of the main fluid parameters with different methane injection temperatures and different injectors on atomization performance and combustion performance. The results show that the larger propellant momentum ratio and Weber number can improve the heat flux and combustion stability in shear coaxial injector, while the influence in swirl coaxial injector is relatively small. Moreover, in shear coaxial injector and in swirl coaxial injector, the larger propellant momentum ratio and Weber number can reduce the droplet size, enhance atomization performance, and improve the combustion efficiency. The numerical model provides an economical method to evaluate the main fluid parameters and proposes new design principles of injectors in LOX/methane engine.

1. Introduction

In recent years, the reusable launch vehicle (RLV) has become the spotlight of aerospace industry, and the LOX (liquid oxygen)/methane rocket engine is considered its appropriate power [1–3]. As a propellant for rocket engine, methane has many advantages such as low carbon deposition, low cost, high specific impulse, and environmental protection [4–7]. Because of the importance in liquid rocket engine, many experimental and numerical researches have been done on injectors in recent years [8–10]. The shear coaxial injector combines simple structure with high reliability, while the swirl coaxial injector has better droplet mixing and atomization ability, and they are suitable for gas-liquid injector and liquid-liquid injector in rocket engine [2, 11].

Various studies have been conducted on injectors in LOX/methane engine. Yatsuyanagi [12] found the optimal design for the injector geometry parameters in shear coaxial injector by investigating the combustion stability and the combustion efficiency. Because the heat flow is an important

indicator of the thermal protection design, Song and Sun [13] evaluated the influence of recessed length on wall heat loads with shear coaxial injector, and the results showed the injector recesses raised the heat flux. In addition, the atomization performance is a significant indicator for evaluating the capability of the injector, which can be represented by the size and spatial distribution of the droplet; many related studies have been carried out [14]. Sauter mean diameter (SMD) is a kind of average particle size and is widely recognized. Through the optical technique, Banning et al. [15] and Kim and Yoon [16] all found that SMD declines when the fuel injection temperature increases, and the superheat of fuel can significantly decrease SMD. The above works show that combustion efficiency, heat flux, combustion stability, and atomization performance can be important indicators in the investigation of the injector.

The numerical analysis has been a good addition to the experimental research, and the computational fluid dynamics (CFD) is also an efficient approach [17–19]. Yu et al. [20] applied the 13-component and 20-step reaction mechanism

to investigate an oxygen/methane engine, and the results are consistent with experimental data. Popov et al. [21] investigated the triggering of transverse combustion instability with a nonlinear wave model, which showed a good accuracy. To exactly calculate the heat transfer between the chamber wall and hot gas/coolant is difficult by numerical simulation. Zhang et al. [22] simulated the flow fields with a steady diffusion flamelet model, and the numerical results showed an agreement with the experimental results. Through experimental analyses and numerical simulations, Zhang et al. [23] verified the accuracy of the numerical model to investigate the mechanism of mixing and atomization of the injector. Consequently, the numerical simulation is suitable for analyzing the effect of the fluid parameters on combustion performance and atomization performance.

Focusing on injector, Yang et al. [24, 25] obtained that the variation of momentum flux ratio and fluid state of injector with different methane injection temperatures had an evident effect on flow evolution. Through the experiments, Tian et al. [26] found that the methane injection temperature at 217 K may be the critical temperature, while the combustion was stable at 234 K in a subscale LOX/methane engine. It has been widely accepted that the main fluid parameters have a great influence on combustion and atomization performance. However, the effect of the main fluid parameters on combustion and atomization performance with different methane injection temperatures and different injectors needs more consideration, especially under supercritical state.

In the previous work [10], we studied the influence of injector structure parameters on combustion performance with constant methane injection temperature. In this paper, however, a new three-dimensional numerical model is provided to study the effect of the main fluid parameters on combustion performance and atomization performance. As we know, the fluid parameters will change with the properties of the propellant and the injector structure parameter. This paper analyzes the influence of the main fluid parameters on combustion efficiency, heat flux, combustion stability, and atomization of a LOX/methane engine with different methane injection temperatures and different injector parameters. And the design criteria of the injector structure parameter in our previous work [10] are analyzed with different methane injection temperature conditions to extend their applicable scope. This paper is organized as follows: in Section 2, the method, setup, and validation of the model are presented; Section 3 analyzes the effect of different fluid parameters on combustion performance and atomization performance; eventually, Section 4 summarizes the conclusions.

2. Methods

2.1. Governing Equations and Numerical Model. The governing equation is the three-dimensional Reynolds-averaged Navier-Stokes (RANS) equation in the Eulerian coordinate system, including continuity, momentum, and energy equations [27, 28].

$$\begin{aligned}\nabla \cdot (\rho u) &= 0, \\ \nabla \cdot (\rho u_i u) &= -\nabla P + \nabla \cdot \tau_{\text{eff}}, \\ \nabla \cdot [(\rho E + P)u] &= \nabla \cdot [\lambda_{\text{eff}} \nabla T - (\tau_{\text{eff}} u)],\end{aligned}\quad (1)$$

where λ_{eff} and τ_{eff} are the effective conductivity and the deviatoric stress tensor.

Using ANSYS FLUENT software in this simulation, the standard $k - \varepsilon$ (SKE) turbulence model is applied to solve the turbulent flow with the source phase of the gas-liquid interaction considering the coupling between the gas and the liquid [10]. Using the simplified mechanism of methane combustion including 13 components and 18 steps, the eddy dissipation concept (EDC) model is combined with a density-based coupling algorithm to simulate the reaction [29]. In the EDC model, the reactions are assumed occurring within the fine scales, which means the small turbulent structures, so the corresponding volume fraction is calculated as follows [30, 31]:

$$(\xi^*)^3 = (C_\xi)^3 \left(\frac{\nu \varepsilon}{k^2} \right)^{3/4}, \quad (2)$$

where ξ^* is the length of the fine scales, $*$ denotes the fine-scale quantities, and ν is the kinematic viscosity, and the volume fraction constant C_ξ is set as 2.1377. It is assumed that the species react in the fine structures over a time scale τ^* , when the production rate of component i is R_i .

$$\begin{aligned}\tau^* &= C_\tau \left(\frac{\nu}{\varepsilon} \right)^{1/2}, \\ R_i &= \frac{\rho (\xi^*)^2}{\tau^* [1 - (\xi^*)^3]} (Y_i^* - Y_i),\end{aligned}\quad (3)$$

where C_τ is a time scale constant equal to 0.4082 and Y_i^* is the fine-scale species mass fraction after reacting over the time τ^* . The production rate over τ^* is calculated by the Arrhenius expression. And the in situ adaptive tabulation (ISAT) algorithm is used for the numerical integration operations in the EDC model [32].

It is assumed that the multicomponent gas phase mixture obeys the Soave-Redlich-Kwong (SRK) equation of real gas state and meets the local thermodynamic equilibrium assumption [13, 33]. Properties of the hot gas, including the density, viscosity, specific heat at constant pressure, and thermal conductivity, are calculated by the methods in References [24, 34, 35].

For better efficiency, the calculation for heat transfer in the thrust chamber with regenerative cooling is divided into two regions: the combustion chamber and the cooling channel. The coupled heat transfer model and the combustion instability evaluation model in our previous study [10] are adopted in this paper to calculate the coupling heat transfer and evaluate the combustion instability. A manually iterative procedure is used to couple the two regions, and the iteration procedure is specified in Figure 1. Moreover, the heat flux

and temperature in each cell on the coupling boundary in the combustion region are the same with that in the cooling region.

- (1) The initial temperature distribution of the chamber wall is set on the coupling boundary with the one-dimensional thermodynamic calculation
- (2) Achieving the heat flux distribution between the hot gas and the chamber wall in the combustion region
- (3) The heat flux distribution is set on the coupling boundary in the cooling region channel to acquire, and the new temperature distribution on the coupling boundary is acquired
- (4) Setting the new temperature distribution on the coupling boundary in the combustion region, and calculating the residual error, which means the difference between the two distributions. The iteration of step (2) to step (4) continues until the heat flux is nearly unaltered

The heat conduction inside the thrust chamber wall is governed by Fourier's equation, and the convective heat transfer is calculated with a modified standard wall function method.

$$\nabla \cdot (\lambda \nabla T) = 0, \quad (4)$$

$$q_c = \frac{(T_w - T_f) \rho c_p C_\mu^{1/4} k_p^{1/2}}{T^*},$$

where T^* and k_p mean the nondimensional temperature and the turbulent kinetic energy, respectively.

Treating the instantaneous pressure by fast Fourier transform (FFT), the combustion stability is analyzed, when the inlet is imposed with sinusoidal disturbance.

$$m(x, y, z, t) = \bar{m}(x, y, z, t)[1 + K \sin(2\pi f(t - t_c))], \quad (5)$$

where the amplitude K and the frequency f are set as 2.0 and 50 Hz, respectively, in this study.

2.2. Droplet Evaluation Model. For the liquid phase, the trajectories of droplets are calculated in the Lagrangian coordinate system with the particle orbit method. A planar atomization model is applied to the inlet of liquid oxygen, where the droplet size follows the Rosin-Rammler distribution [20]. Mass fraction of the droplet with diameter greater than d is given as follows:

$$Y_d = e^{-(d/\bar{d})^{n^*}}, \quad (6)$$

where Y_d is the mass fraction and \bar{d} and n^* are the size constants and the size distribution parameters, respectively, which are set to 0.01 mm and 3.5 as default.

It is the relative velocity of the gas and the liquid that breaks the droplets in the wave breakup model, which is appropriate for high-Weber number flows and high-speed

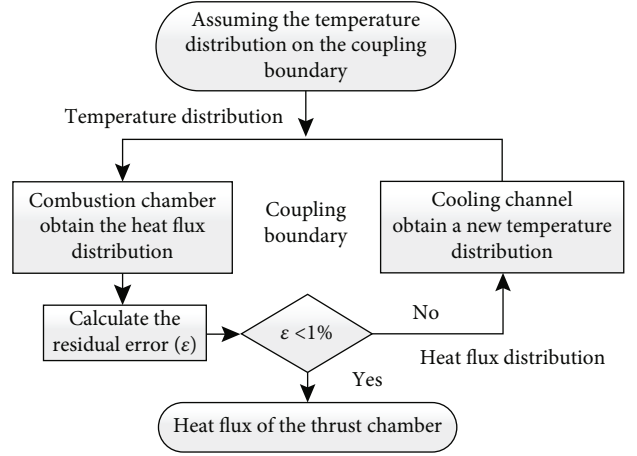


FIGURE 1: Schematic of the iteration procedure.

injections, where the breakup of droplets is dominated by the Kelvin-Helmholtz instability [36]. The time scale of the breakup and the corresponding sizes of the droplets are assumed related to the fastest-growing Kelvin-Helmholtz instability, where the characteristics of the newly formed droplets are predicted using the wavelength and the growth rate. The radius of the newly formed droplet is assumed proportional to the wavelength of the fastest-growing unstable surface wave on the parent droplet as shown in Equation (7). The rate of change of droplet radius in the parent parcel is given as Equations (8) and (9).

$$r = B_0 \Lambda, \quad (7)$$

$$\frac{da}{dt} = -\frac{(a-r)}{\tau}, \quad r \leq a, \quad (8)$$

$$\tau = \frac{3.726 B_1 a}{\Lambda \Omega}, \quad (9)$$

where B_0 and B_1 are the model constants and the time constant of breakup, respectively, which are set as 0.61 and 1.73 according to Reference [36] and Reference [37], Λ is the corresponding wavelength given in Reference [36], a is the radius of the liquid jet, τ is the time scale of breakup, and Ω is the maximum growth rate.

Furthermore, the two nondimensional parameters, propellant momentum ratio and Weber number, are given as follows:

$$Mr = \frac{m_f v_f}{m_o v_o}, \quad (10)$$

$$We = \frac{\rho_f (v_f - v_o)^2 d_l}{\sigma_o},$$

where m_f and m_o are the mass flow rate of methane and LOX, v_f and v_o are the velocity of methane and LOX, ρ_f is the density of methane, σ_o is the coefficient of surface tension for LOX, and d_l is the characteristic length.

TABLE 1: The fluid and structure parameters of each case.

Case	Methane temperature (K)	Coaxial injector type	LOX post thickness (δ) (mm)	Injector number	Mr	We	D_1 (mm)	Re_f	Re_o
Case 1	200	Shear	0.25	12	2.06	278.9	8.0	371321	467803
Case 2	200	Shear	0.35	12	2.06	278.9	8.0	362657	467803
Case 3	200	Shear	0.50	12	2.06	278.9	8.0	346567	467803
Case 4	200	Shear	1.00	12	2.06	278.9	8.0	315623	467803
Case 5	200	Swirl	0.25	12	1.26	212.6	6.1	389887	581628
Case 6	200	Shear	0.25	18	2.05	219.6	6.3	433208	368395
Case 7	234	Shear	0.25	12	4.41	544.7	8.0	723501	467803
Case 8	234	Swirl	0.25	12	2.70	415.4	6.1	759676	581628

TABLE 2: Parameters of injector arrangement.

No.	Injector number	LOX post thickness (δ) (mm)	D_1 (mm)	D_3 (mm)	D_4 (mm)	D_5 (mm)	D_6 (mm)
Case 1	12	0.25	8.0	15	113	46	89
Case 6	18	0.25	6.3	12.25	113	46	89

In this study, the discrete phase model (DPM) is adopted, and the droplet evaluation model refers to methods in Reference [23].

2.3. Model Setup and Boundary Condition. The model used in this study is based on the subscale LOX/methane rocket engine in Reference [26]. Boundary conditions at methane and LOX inlets are composed of temperature, mass flow rate, and initial pressure. The oxygen/fuel ratio is set to 3.6, and the temperature of LOX is set to 98 K.

To evaluate the influence of fluid parameters with different methane injection temperatures and injector parameters on atomization performance and combustion performance, six new cases with methane injection temperature at 200 K are solved with different configurations such as thickness of the LOX posts, types and number of the injector, and other settings shown in Table 1. The effect of different thicknesses of LOX posts is analyzed by Case 1 to Case 4. Comparison between Case 1 and Case 6 is used to analyze the effect of injector number, and the parameters of two kinds of injector arrangement are shown in Table 2. Comparison between Case 1 and Case 5 is used to analyze the effect of injector types.

Moreover, the density, viscosity, specific heat, and some other properties of methane will change drastically with temperature. The injection temperature of 234 K for methane is recommended in Reference [26]. As methane becomes supercritical when the temperature goes above 190 K under high pressure, 200 K and 234 K are chosen as the methane injection temperatures for comparison in the present work. Therefore, Case 7 and Case 8 with methane injection temperature at 234 K, which have the same working condition as the case in our previous work [10], are chosen to study the impact of the fluid parameters with different methane injection temperatures in the shear coaxial injector and in swirl coaxial injector by comparing with Case 1 and Case 5.

The engine model with 12 injectors and the schematic of coaxial injector are shown as Figure 2, where δ means the thickness of the LOX post. Because the geometry of the engine is periodical along the circumferential direction, a 45 degree in Case 1 to Case 4 and Case 7, a 30 degree in Case 6, and a 90 degree in Case 5 and Case 8 of thrust chamber are taken as computational domains. The structural grid is used for spatial discretization with appropriate refinement near the outlet of injectors for raising the grid quality.

2.4. Model Validation. In our previous work [10], part of the model has been verified by comparison with experiments in References [26, 38]. The combustion model and the combustion instability evaluation model are verified with experiments by Beijing Aerospace Propulsion Institute (BAPI) [26] in Figure 3(a), where the subplots show the FFT results with dynamic injection pressures. The coupled heat transfer model is validated by a comparison between our numerical simulation and the experiment done by Locke et al. [38] at different chamber pressure conditions in Figure 3(b), where the numerical simulation results obtained by Song and Sun [13] are also used for comparison. The grid convergence analysis is performed by comparing the numerical simulation results of the wall temperature at different grid levels in Table 3. As Figure 4 shows, the solution using the base grids is independent of the adopted grid. In addition, using the methods in References [39, 40], the accumulated error in the transient simulation of the combustion instability evaluation model has been calculated, which is less than 1.5%, and the reliability is more than 12.6, also validating the combustion stability analysis with the adopted grid.

The droplet evaluation model used in this study refers to the model established by Zhang et al. [23], which has been validated by comparison with the experiments in Reference [41].

In conclusion, satisfying consistency between the results of existing experiments and our numerical simulation proves the accuracy of the model established in this paper. The

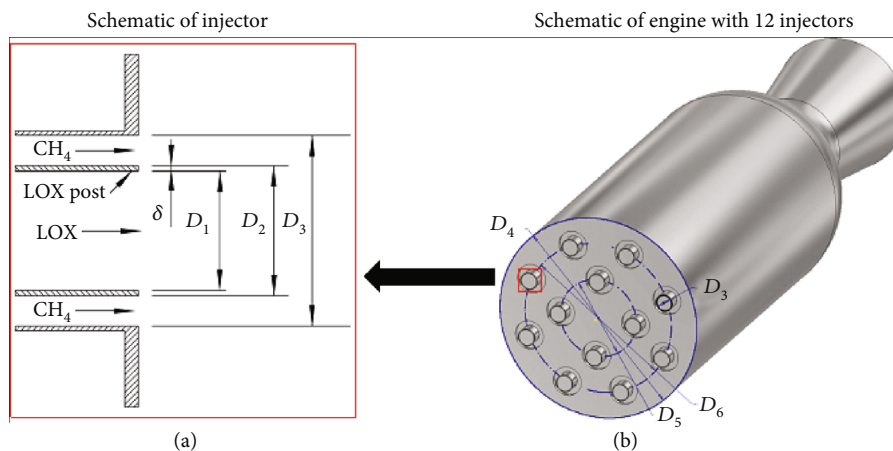


FIGURE 2: Schematic of engine model and injector.

model will be applied to evaluate the effect of fluid parameters with different methane injection temperatures and different injector parameters on combustion performance and atomization performance.

3. Results and Discussion

The eight cases with different fluid parameters are carried out, and the results show that fluid parameters such as the propellant momentum ratio, the Weber number, and the Reynolds number have noticeable influence on combustion and atomization characteristics. In the following part, the combustion efficiency, heat flux, combustion stability, and atomization performance are discussed, respectively.

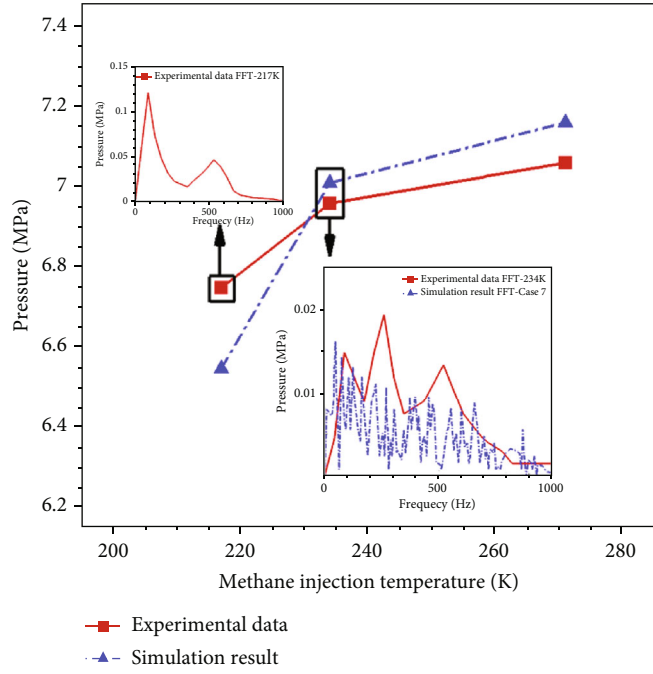
3.1. Combustion Efficiency. The correlation between combustion efficiency and propellant fluid properties is studied by the chamber pressure from Case 1 to Case 8, which share the same total mass flow rate. Methane's Reynolds number varies from Case 1 to Case 4 by changing the LOX post thickness. As the LOX post thickness in Case 4 increases four times comparing to Case 1, the Reynolds number of methane decreases by 15.0%. The pressure declines by 3.98% from ~ 7.03 MPa (Case 1) to ~ 6.75 MPa (Case 4) (see subplot in Figure 5(a)). This is because the reduction of the methane's Reynolds number weakens the mixing of propellants, which further leads to a decline of atomization and combustion efficiency. It can be observed in Figure 5(a) that the changes in propellant momentum ratio and the Weber number with different injector types almost have no influence on combustion efficiency. According to Table 1, when the injection temperature rises from 200 K to 234 K, the propellant momentum ratio and the Weber number rise, which result in the increase of chamber pressure in shear coaxial injectors from ~ 7.03 MPa (Case 1) to ~ 7.10 MPa (Case 7), while the chamber pressure in swirl coaxial injectors (Case 5 and Case 8) is basically the same. Hence, the propellant momentum ratio and the Weber number hardly influence the combustion efficiency.

The mass fraction of water, which can be used for combustion performance evaluation, is also investigated,

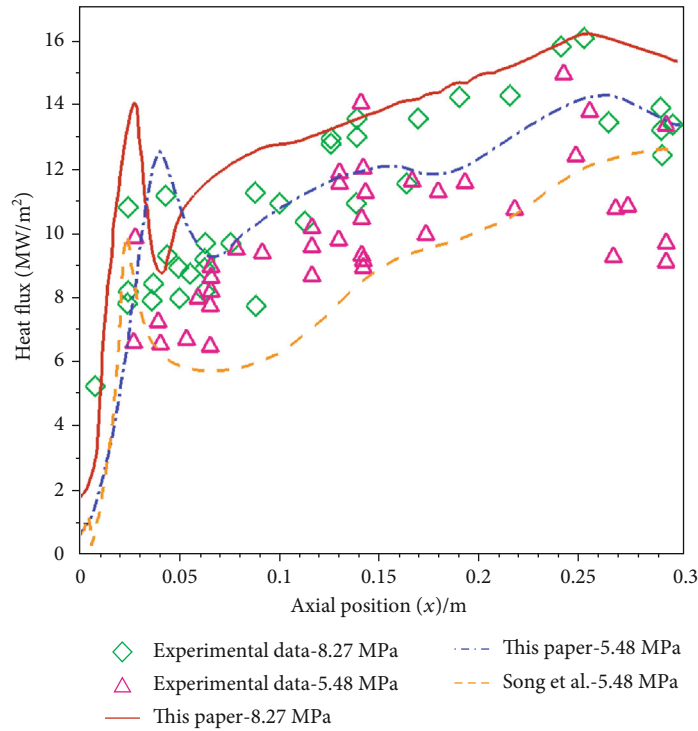
as shown in Figure 5(b). The products accumulate in the recirculation zone results in a higher water mass fraction near the injection panel with the minimum level at $x = 0.05$ m in Case 1. The water mass fraction rises rapidly downstream between $x = 0.05$ m and $x = 0.20$ m, indicating the main combustion region. From there on, the water mass fraction rises gradually and reaches 38.9% at the outlet of the nozzle. According to the definition of combustion length, the axial distance from the injection panel to where the water mass fraction is 90% of the ideal condition, that is, 38.14% in this model as indicated by the dotted red line in Figure 5(b). The trends in Case 2, Case 3, Case 4, and Case 7 are basically the same as Case 1. Nevertheless, when the Reynolds number of methane declines as the thickness of the LOX post increases, the water mass fraction declines at the corresponding axial position, and the combustion length increases gradually. When the Reynolds number of methane in Case 4 decreases by 15.0% comparing to Case 1 as the LOX post thickness increases four times, the minimum water mass fraction at $x = 0.05$ m declines by 48.29%. As the propellants are not fully reacted in Case 4, the combustion efficiency declines.

Compared to the results of shear coaxial injector mentioned above, we can find that the water mass fraction rises rapidly adjacent the injection panel and then grows smoothly using the swirl coaxial injector, which results from the absence of the recirculation zone (Case 5 and Case 8). When the propellant momentum ratio and the Weber number increase as the injection temperature changes from 200 K to 234 K, the water mass fraction rises at the corresponding axial position. The combustion length in Case 8 is 47.63% shorter than that in Case 1, so the length and the weight of the chamber can be reduced with swirl coaxial injector as a benefit. From the results of water mass fraction, the propellants have complete combustion in Case 1, Case 5, Case 7, and Case 8; thus, the pressure is almost the same in Figure 5(a).

Investigation on the influencing factors on combustion efficiency suggests that a decrease of methane's Reynolds number resulting from an increase in the LOX post thickness



(a) The pressure curves and FFT results



(b) The wall heat flux curves

FIGURE 3: The comparison between experimental data and simulation result.

TABLE 3: Various grid arrangements.

Grid types	Methane injector	LOX injector	Thrust chamber	Cooling channel
Coarse grids	2 × 5 × 80	12 × 10 × 80	40 × 20 × 70	40 × 12 × 70
Base grids	4 × 10 × 90	18 × 15 × 90	60 × 25 × 80	60 × 16 × 80
Fine grids	6 × 15 × 100	24 × 20 × 100	80 × 30 × 90	80 × 20 × 90

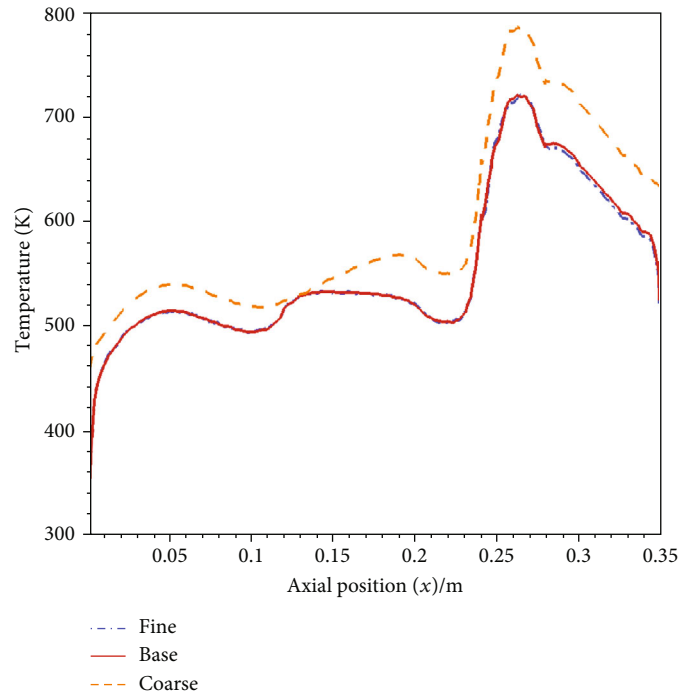


FIGURE 4: The numerical result of temperature distribution and streamlines.

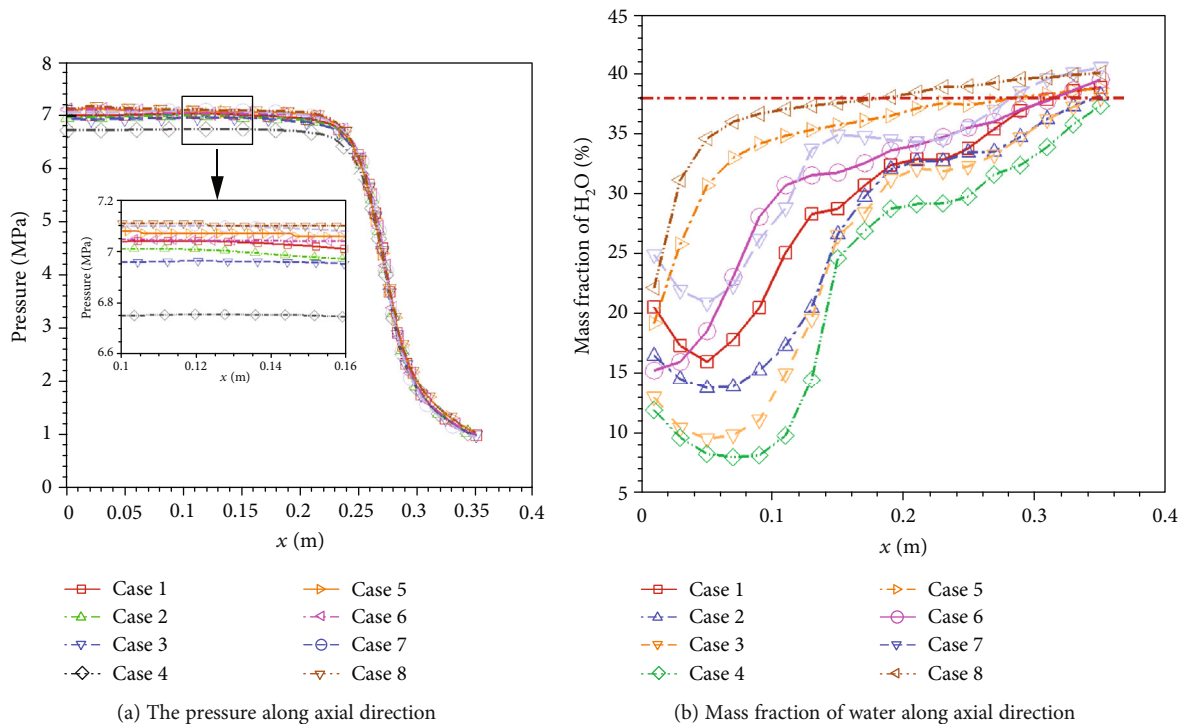


FIGURE 5: The numerical results of combustion efficiency analysis.

can bring a decrease in the combustion efficiency nonuniformly. However, analysis of the effect of different injection temperatures shows that the propellant momentum ratio and the Weber number have almost no influences on the combustion efficiency, while the two parameters are negatively correlated with the combustion length.

3.2. *Heat Flux.* In Figure 6(a), we have demonstrated the heat flux diagram along the axial direction. The axial heat flux in Case 1 rises from the injection panel to $x = 0.07$ m, then drifts slightly before the nozzle, where the cross-sectional area of the thrust chamber contracts sharply in the convergent part of the nozzle with the axial heat flux rising drastically and

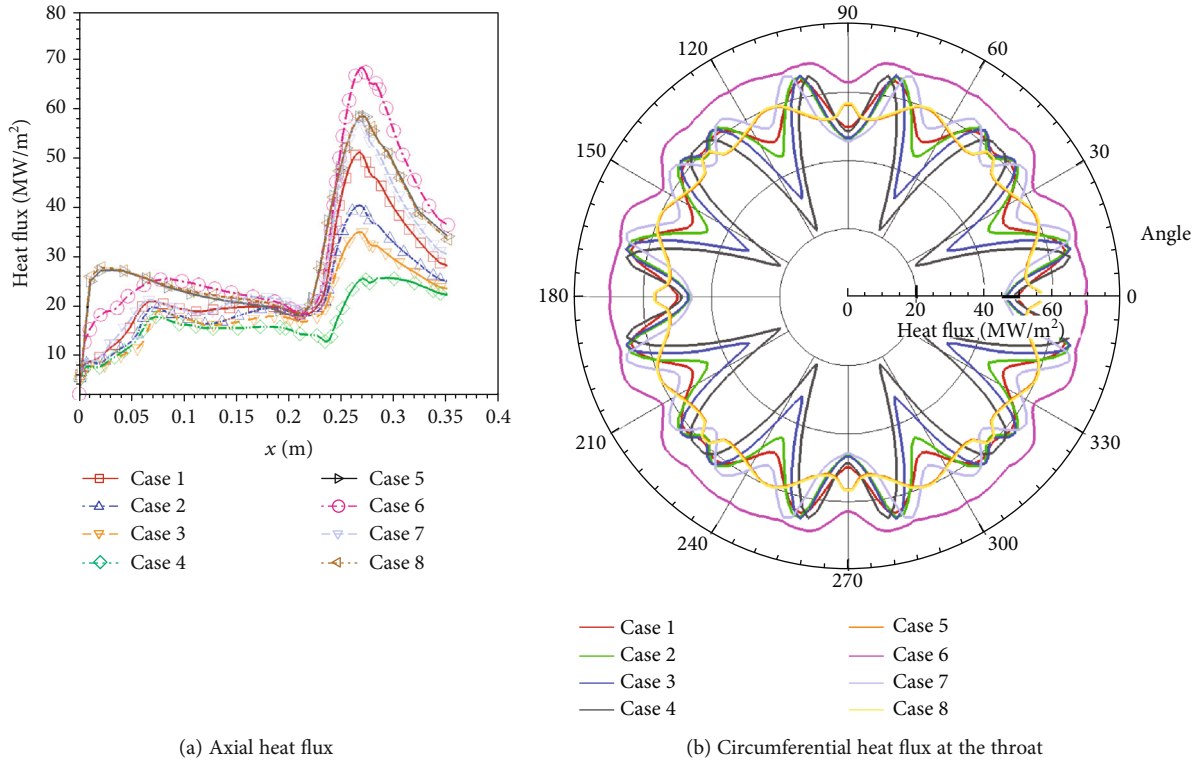


FIGURE 6: The numerical results of heat flux analysis.

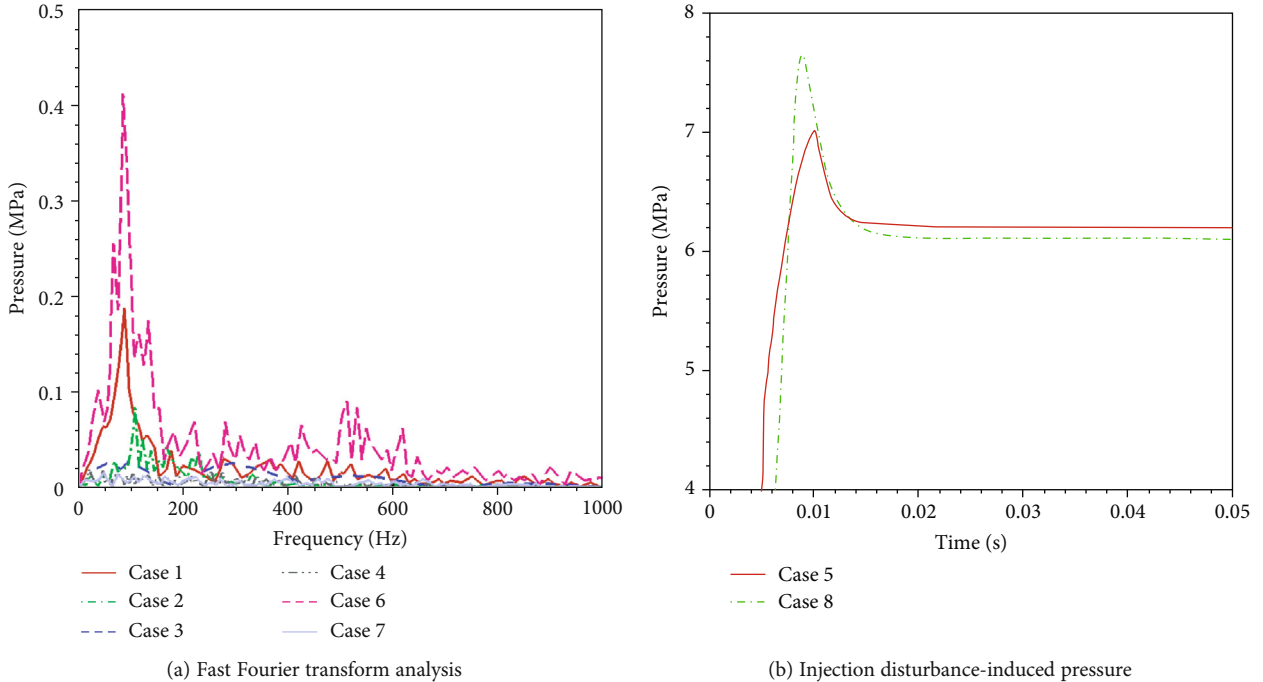


FIGURE 7: The numerical results of combustion stability analysis.

reaching the maximum near the throat. In the expansion part of the nozzle, the axial heat flux declines as the cross-sectional area enlarges. The similar trend is observed in Case 2 to Case 4 as well. However, as the Reynolds number of methane declines with the increase of LOX post, the axial

heat flux value declines at the corresponding axial position. In Case 4, where the LOX posts are four times thick as that of Case 1, the maximum axial heat flux decreases by 49.81%. Such difference can also be interpreted by the incomplete combustion which has already been discussed in

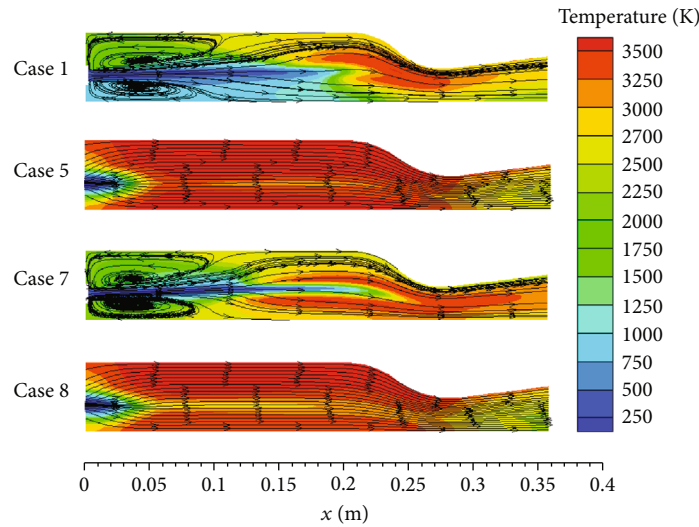


FIGURE 8: The numerical result of temperature distribution and streamlines.

Figure 5(b). In Case 4, the propellants do not react completely before the throat, leading to less heat release by combustion. Moreover, the incompletely reacted low-temperature gas flow absorbs more energy from high-temperature products, which further reduces the heat flux.

The circumferential heat flux at the throat is shown in Figure 6(b), which has a period of 90° in the polar coordinate depending on the arrangement of the injection panel. The inner and outer injectors are set at intervals of 90° and 45° , respectively, in Case 1, and the variation of circumferential heat flux at the throat is small as the result of complete combustion. Moreover, the minimum heat flux appears periodically on the symmetric line of every two adjacent outer injectors due to the cooling effect of the unreacted oxygen. Comparison between Case 1 and Case 4 shows a similar trend of circumferential heat flux with almost the same maximum value. However, when the Reynolds number of methane decreases from Case 1 to Case 4, the minimum value of circumferential heat flux declines. In Case 4, we observe a drop of circumferential heat flux by 56.67% as the methane's Reynolds number decreases 15% compared to Case 1.

The trends of axial heat flux are different between the swirl and the shear coaxial injectors. Axial heat flux in swirl injectors rises quickly nearby the injection panel and is 280% larger in Case 5 at $x = 0.2$ m than that in Case 1. This is because of the radial movement of LOX in swirl coaxial injector, which moves the mixing and combustion position closer to the injection panel, while this is one of the deficiencies of swirl coaxial injector as high temperature nearby the injection panel may cause thermal damage to its structure. The axial heat flux in Case 5 decreases due to the cooling channel before the convergent part of the nozzle and reaches maximum at the throat with a 20.80% rise compared with Case 1. As shown in Figure 6(b), the circumferential heat flux at the throat is almost the same in the polar coordinate in Case 5 and Case 8 because of the complete combustion of the propellants.

The effect of temperature on heat flux is evaluated by examining the data of Case 1, Case 5, Case 7, and Case 8 in Figure 6. The propellant momentum ratio and the Weber number increase as the methane injection temperature rises from 200 K to 234 K. The axial heat flux does not change obviously in swirl coaxial injector, while in shear coaxial injector, it increases in the convergent part of the nozzle and the maximum rises 13.46% in Case 7 compared to the value in Case 1 as the result of the completeness of combustion. When the methane injection temperature rises, the momentum ratio and the Weber number increase as the methane velocity increases, which strengthens the mixing of the propellant making the combustion efficiency in Case 7 higher than that in Case 1. Furthermore, the maximum and minimum circumferential heat flux at the throat rises by 4.02% and 8.43%, respectively, in Case 7 compared to Case 1, while this is not the case with a swirl coaxial injector.

By analyzing the heat flux under different injection conditions, it is found that when the Reynolds number of methane declines as the LOX post thickness enlarges, the axial and circumferential heat flux declines. Additionally, the swirl coaxial injector makes the combustion region nearby the injection panel and increases the heat flux, which results in higher requirement for thermal protection of the structure. When the propellant momentum ratio and the Weber number increase with elevated methane injection temperature, the axial and circumferential heat flux rises in the thrust chamber using shear coaxial injectors, while the phenomenon is not obvious using swirl coaxial injectors.

3.3. Combustion Stability. The combustion instability evaluation model is applied to investigate the impact of propellant fluid properties on combustion stability. With an injection disturbance, the combustion is more stable with larger LOX post thickness, as shown in Case 1-Case 4 in Figure 7(a). There is no combustion oscillation phenomenon in all cases, so the declined Reynolds number of methane almost has no

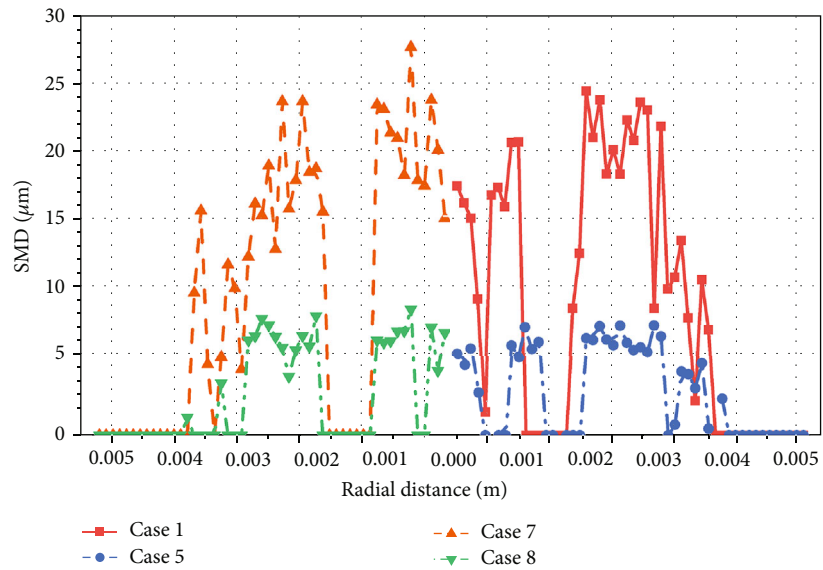
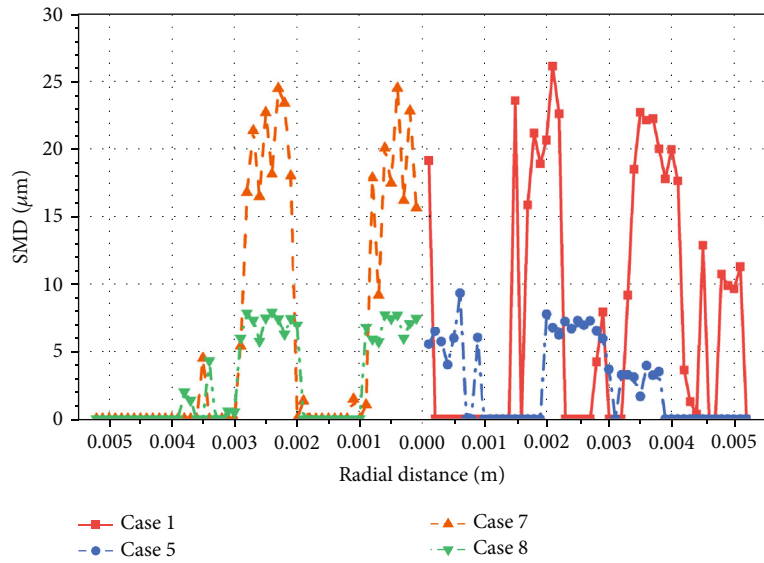


FIGURE 9: Continued.

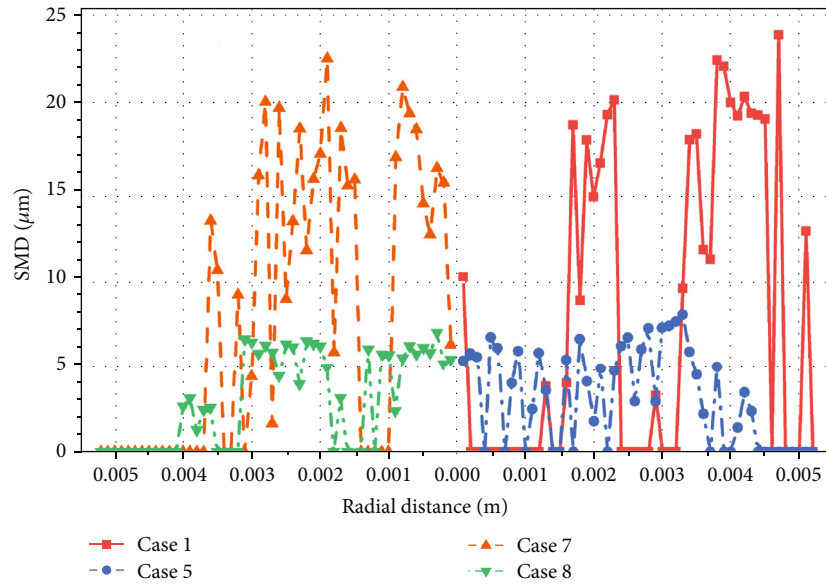
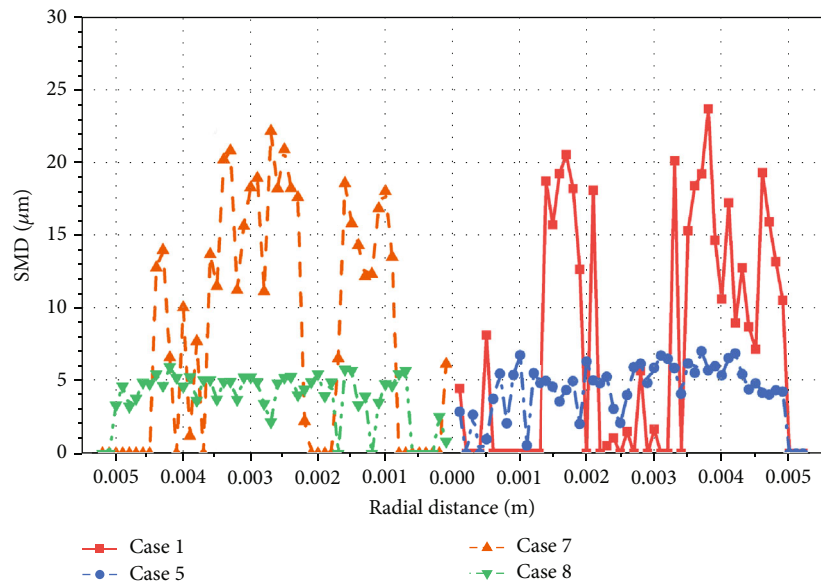
(c) Axial position at $x/D = 1/2$ (d) Axial position at $x/D = 1$

FIGURE 9: Comparison of the SMD distribution radial direction at the same axial position in different cases.

obvious impact on combustion stability, which is consistent with the conclusions in Reference [42]. To analyze the effect of injector number on combustion stability, comparison between Case 6 and Case 1 is conducted, while the former has more injectors, larger LOX's Reynolds number and Weber number. The FFT result shows that there is a 100 Hz low-frequency oscillation with the amplitudes of 0.4 MPa. As there are more injectors, the recirculation area shrinks and the combustion stability weakens.

To compare the combustion stability of the two injector types, we also impose injection disturbances on mass flow rate to swirl coaxial injectors (Case 5 and Case 8). In Figure 7(b), the thrust chamber pressure is stable, i.e., stable combustion, so there is no need for FFT processing. Furthermore, the increased propellant momentum ratio and Weber

number, as the result of risen methane injection temperature, have no obvious effect on combustion stability especially for in swirl coaxial injector.

By analyzing the combustion stability with different propellant fluid properties, it is found that the Reynolds number of methane, the propellant momentum ratio, and the Weber number have little effect on combustion stability for either shear coaxial injector or swirl coaxial injector. Instead, the scale of the recirculation zone, varying with the Reynolds number of LOX and the velocity of propellants, may have influence on the combustion stability.

3.4. Atomization Performance. In order to analyze the impact of propellant fluid properties on atomization, 4 cases (Case 1, Case 5, and Case 7 to Case 8) of two injector types are

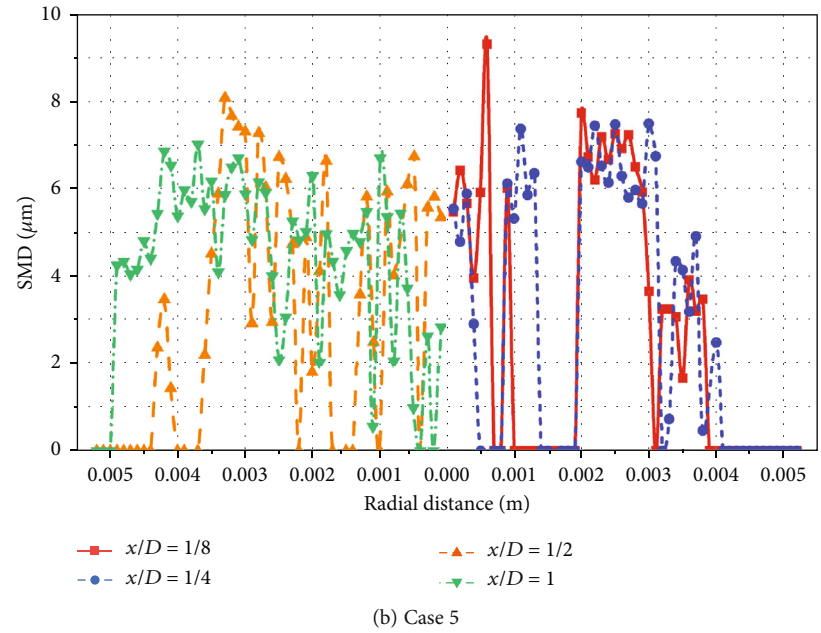
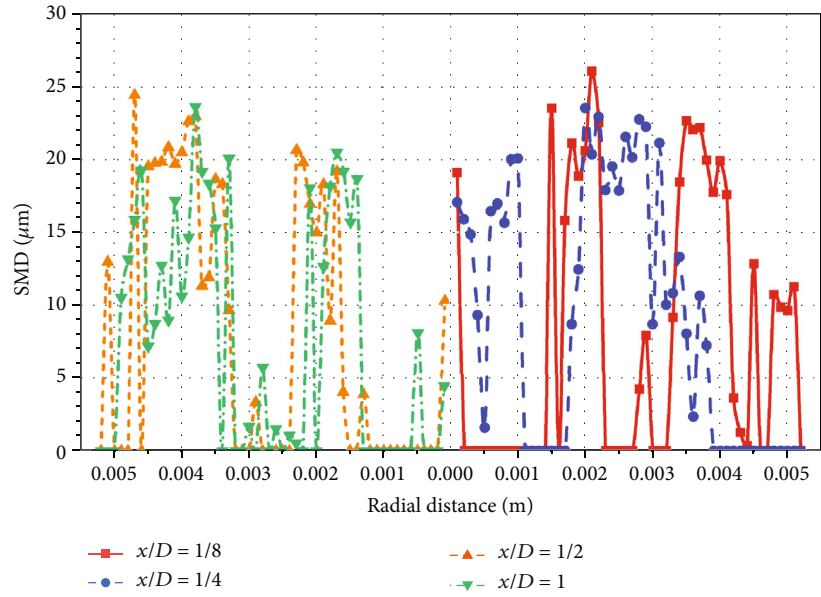
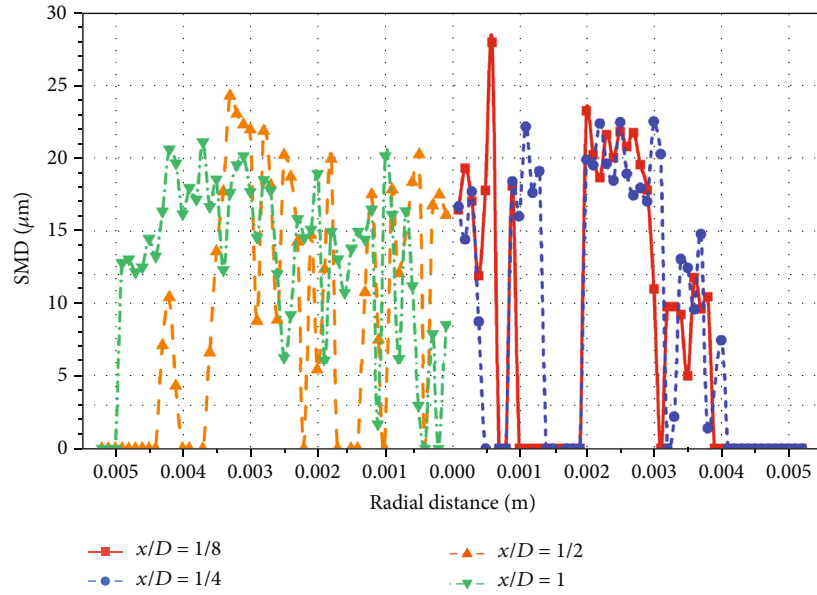
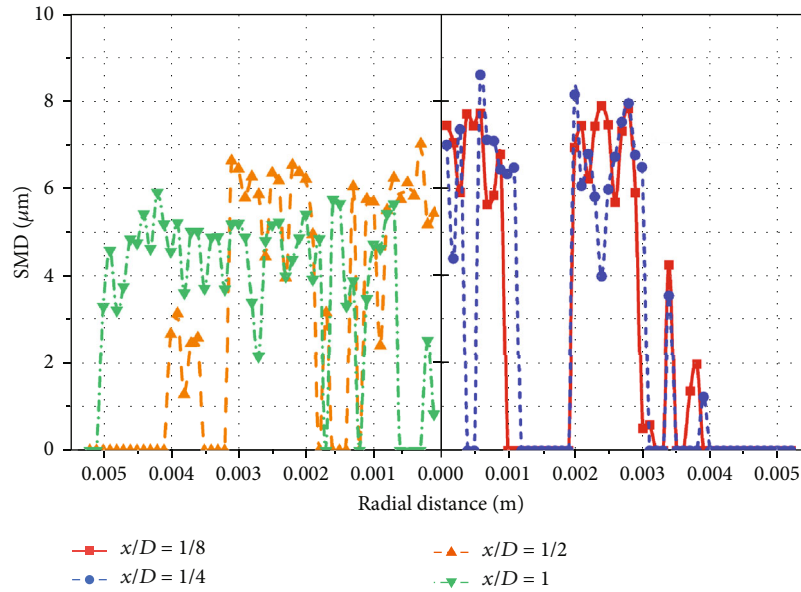


FIGURE 10: Continued.



(c) Case 7



(d) Case 8

FIGURE 10: Comparison of the SMD distribution along radial direction in specific case at different axial positions.

investigated with same velocity magnitude and total mass flow rate. As shown in Figure 8, the streamlines and the temperature contours of the longitudinal center plane of the chamber in different cases are compared. Shear coaxial injectors are used in Case 1 and Case 7, and swirl coaxial injectors are used in Case 5 and Case 8. In Figure 8, the expansion of the combustion reaction area nearby the injection panel can be verified, corresponding to the analysis of water mass fraction in Section 3.1. The propellants injected in Case 5 and Case 8 have radial velocity, which brings better mixing than Case 1 and Case 7. Meanwhile, in Case 5 and Case 8, the recirculation zone disappears and when the temperature is higher, the flow is more stable. In addition, although the methane injection temperature varies, the effect of propel-

lant momentum ratio and Weber number on the streamline is negligible.

The distribution characteristic of the Sauter mean diameter (SMD) is analyzed for evaluation of the droplet. The SMD can be expressed as follows:

$$\text{SMD} = \frac{\sum_{ii=1}^{n_s} d_{ii}^3}{\sum_{ii=1}^{n_s} d_{ii}^2}, \quad (11)$$

where d_{ii} represents the diameter of the ii -th particle.

The results are calculated using the following computing method and shown in Figures 9 and 10. In axial direction, some cross sections with an interval of $dx = 1 \text{ mm}$ are taken

and divided into one circular and several annular multiple subregions with same radial width of $dr = 1$ mm. The SMD of each subregion is computed by Equation (11).

The SMD distributions along the radial direction at $x = 0.013$ m ($x/D = 1/8$), $x = 0.026$ m ($x/D = 1/4$), $x = 0.052$ m ($x/D = 1/2$), and $x = 0.104$ m ($x/D = 1$) downstream the injection panel are shown in Figure 9. The mixing zones have unique characteristics. As we can see from Figures 9 and 10 that the value of the SMD near the centerline and injectors is larger due to the recirculation zone and the insufficient fragmentation of the droplets, respectively; SMD in other regions is smaller. As shown by comparing the value of SMD at the four selected axial positions, the droplet diameter gradually decreases along the axial direction due to the atomization, collision, and breakup of the droplets. It can be seen that the atomization performance of the swirl coaxial injector is obviously better than the shear coaxial injector. The SMD is reduced by nearly 75%. The droplet diameter in the swirl coaxial injector distributes uniformly in radial direction at the axial position $x = 0.052$ m due to the radial velocity, indicating that the droplets from the inner and outer injector have mixed with each other. In the shear coaxial injector, the droplet diameter at smaller radius decreases as the axial distance increases. When the axial position reaches $x = 0.104$ m, the diameter of droplets in the middle of the thrust chamber reduces significantly, indicating that the droplet has left the recirculation zone in Figure 8.

Figure 10 compares the SMD of the shear coaxial injector in Case 1 and Case 7 with the swirl coaxial injector in Case 5 and Case 8. When the propellant momentum ratio and the Weber number increase as methane injection temperature rises, the overall value of SMD decreases. However, the SMD increases near the center of the thrust chamber. Moreover, the droplets become more concentrated and decrease near the combustion chamber wall. As the density of methane decreases with the increase of temperature, the methane injection speed increases, so the high-speed methane takes the liquid oxygen droplets farther downstream, enlarging the recirculation zone using the shear injector. Because of the impact of high-speed methane, the breakup effect of the liquid oxygen droplet is strengthened, and the atomization performance is improved. The reduced value of SMD is consistent with the conclusions in Reference [23].

As shown by analyzing the atomization performance in cases with different propellant fluid properties, the diameter of droplets reduces with higher Weber number and propellant momentum ratio. While using swirl coaxial injector, the droplet diameter is reduced by about 75%, indicating a better atomization performance. However, a combustion zone adjacent to the injection panel requires demanding thermal protection for using swirl coaxial injector.

4. Conclusions

This paper establishes a three-dimensional numerical model based on a typical subscale LOX/methane engine, which has been verified by the experiments in the literature. With the help of the new model, numerical cases of different fluid parameters are carried out to analyze their effect on com-

busion performance and atomization performance. The main conclusions drawn from the results are summarized as follows:

- (1) The analysis of combustion efficiency demonstrates that the combustion efficiency declines as the Reynolds number of methane decreases with the increasing LOX post thickness. And the combustion length of the swirl coaxial injector reduces by 47.63% compared to the shear coaxial injector
- (2) The fluid parameters have little effect on combustion stability. Analysis of the effect of different fluid parameters on combustion performance shows that the axial heat flux and circumferential heat flux decline as the Reynolds number of methane decreases. When it declines by 15.0% as the LOX post thickness augments by four times, the maximum axial heat flux declines by 49.81% and the minimum circumferential heat flux reduces by 56.67%. The axial heat flux and circumferential heat flux rise in shear coaxial injector as the propellant momentum ratio and Weber number increase with the rising methane temperature. When propellant momentum ratio rises by 214% and Weber number rises by 250%, the maximum axial heat flux rises by 13.46%, while these two parameters almost have no effect in swirl coaxial injector, but the axial heat flux is 280% bigger near the injection panel in swirl coaxial injector comparing to the shear coaxial injector, which results in higher requirement for the thermal protection of injector structure
- (3) The swirl coaxial injector has better atomization performance than the shear coaxial injector, and the value of SMD is reduced by about 75%. Moreover, when the Weber number and momentum ratio increase as the methane injection temperature rises, the diameter of LOX droplets reduces. According to our previous work and this paper, the effect of LOX post thickness and injector type on combustion efficiency and heat flux in different methane injection temperatures shows the same trend

This model provides a reliable and effective method for analyzing the effect of fluid parameters with different methane injection temperatures and different injector parameters on combustion performance and atomization performance in LOX/methane engine under supercritical state. The research results provide new design principles for the injector structure and the inlet condition in LOX/methane engine, and show that these principles are applicable at different injection temperatures. Future work will be devoted to the analysis of the effect of fluid parameters with different swirl coaxial injector parameters on combustion performance and atomization performance in LOX/methane engine.

Nomenclature

D : Diameter, mm

k_p : Turbulent kinetic energy, m^2/s^2
 P : Pressure, Pa
 T : Temperature, K
 T^* : Nondimensional temperature, K
 x : Axial position, m
 δ : LOX post thickness, mm
 ε : The residual error
 λ : Thermal conductivity, W/(m·K)
 λ_{eff} : Effective conductivity
 ρ : Density, kg/m^3
 τ : Breakup time
 τ_{eff} : Deviatoric stress tensor.

Abbreviations

DPM: Discrete phase model
 EDC: Eddy dissipation concept
 FFT: Fast Fourier transform
 RANS: Reynolds-averaged Navier-Stokes
 RLV: Reusable launch vehicle
 SKE: Standard $k - \varepsilon$
 SMD: Sauter mean diameter
 SRK: Soave-Redlich-Kwong.

Data Availability

The numerical simulation result data used to support the findings of this study are available from the corresponding author upon request.

Conflicts of Interest

The authors declare that they have no known competing financial interests or personal relationships that could have appeared to influence the work reported in this article.

References

- [1] H. Cai, W. Nie, X. Yang, R. Wu, and L. Su, "Three-dimensional numerical analysis of LOX/kerosene engine exhaust plume flow field characteristics," *International Journal of Aerospace Engineering*, vol. 2017, Article ID 4768376, 13 pages, 2017.
- [2] C. GuoBiao, D. Jian, Z. Yang, and Y. NanJia, "Combustion behaviors of GO₂/GH₂ swirl-coaxial injector using non-intrusive optical diagnostics," *Acta Astronautica*, vol. 123, pp. 246–256, 2016.
- [3] M. M. Heydari and N. Ghadiri Massoom, "Experimental study of the swirling oxidizer flow in HTPB/N₂O hybrid rocket motor," *International Journal of Aerospace Engineering*, vol. 2017, Article ID 3174140, 10 pages, 2017.
- [4] D. Greatrix, I. Leyva, D. Pastrone, V. S. Kumar, and M. Smart, "Chemical rocket propulsion," *International Journal of Aerospace Engineering*, vol. 2012, 2012.
- [5] W. Nie, S. Zhou, T. Shi, T. Zheng, and X. Che, "Experimental investigation of CH₄/air inverse diffusion flame stabilization by nonequilibrium plasma," *Journal of Propulsion and Power*, vol. 35, no. 6, pp. 1151–1162, 2019.
- [6] N. Perakis, D. Rahn, O. J. Haidn, and D. Eiringhaus, "Heat transfer and combustion simulation of seven-element O₂/CH₄ rocket combustor," *Journal of Propulsion and Power*, vol. 35, no. 6, pp. 1080–1097, 2019.
- [7] H. Wang, W. Nie, and L. Su, "Experimental investigation of thermodynamic instability of supercritical endothermic hydrocarbon fuel within a small-scale channel," *Advances in Mechanical Engineering*, vol. 11, 2019.
- [8] D. Gao, J. Qin, and H. Zhang, "Investigation on acoustic properties of thruster chamber with coaxial injectors and plenum chamber," *International Journal of Aerospace Engineering*, vol. 2020, Article ID 9672358, 12 pages, 2020.
- [9] X. Jin, C. Shen, R. Zhou, and X. Fang, "Effects of LOX particle diameter on combustion characteristics of a gas-liquid pintle rocket engine," *International Journal of Aerospace Engineering*, vol. 2020, Article ID 8867199, 16 pages, 2020.
- [10] J. Xu, P. Jin, R. Li, J. Wang, and G. Cai, "Effect of coaxial injector parameters on LOX/methane engines: a numerical analysis," *Acta Astronautica*, vol. 171, pp. 225–237, 2020.
- [11] J. Dai, G. Cai, Y. Zhang, and N. Yu, "Experimental investigations of coaxial injectors in a laboratory-scale rocket combustor," *Aerospace Science and Technology*, vol. 59, pp. 41–51, 2016.
- [12] N. Yatsuyanagi, "Comprehensive design method for LOX/liquid-methane regenerative cooling combustor with coaxial injector," *Transactions of the Japan Society for Aeronautical and Space Sciences*, vol. 52, no. 177, pp. 180–187, 2009.
- [13] J. Song and B. Sun, "Coupled heat transfer analysis of thrust chambers with recessed shear coaxial injectors," *Acta Astronautica*, vol. 132, pp. 150–160, 2017.
- [14] L. Liu, L. Yang, and Q. Fu, "Droplet size spatial distribution model of liquid jets injected into subsonic crossflow," *International Journal of Aerospace Engineering*, vol. 2020, Article ID 9317295, 14 pages, 2020.
- [15] D. H. C. Van Banning, C. W. M. Van der Geld, P. J. C. Broos, and M. J. Strebe, "An assessment of nozzles for steam attemperation," *Experimental Thermal and Fluid Science*, vol. 55, pp. 86–94, 2014.
- [16] W. H. Kim and W. S. Yoon, "Spray characteristics of a flash swirl spray ejected into an atmospheric pressure zone," *International Journal of Multiphase Flow*, vol. 39, pp. 1–12, 2012.
- [17] J. Du, F. Lin, J. Chen, S. C. Morris, and C. Nie, "Numerical study on the influence mechanism of inlet distortion on the stall margin in a transonic axial rotor," *Journal of Thermal Science*, vol. 21, no. 3, pp. 209–214, 2012.
- [18] V. P. Zhukov and M. Feil, "Numerical simulations of the flame of a single coaxial injector," *International Journal of Aerospace Engineering*, vol. 2017, Article ID 5147606, 11 pages, 2017.
- [19] Z. Li, J. Du, X. Ottavy, and H. Zhang, "Quantification and analysis of the irreversible flow loss in a linear compressor cascade," *Entropy*, vol. 20, no. 7, p. 486, 2018.
- [20] N. Yu, Y. Zhang, F. Li, and J. Dai, "Numerical and experimental investigations of single-element and double-element injectors using gaseous oxygen/gaseous methane," *Aerospace Science and Technology*, vol. 75, pp. 24–34, 2018.
- [21] P. P. Popov, A. Sideris, and W. A. Sirignano, "Stochastic modelling of transverse wave instability in a liquid-propellant rocket engine," *Journal of Fluid Mechanics*, vol. 745, pp. 62–91, 2014.
- [22] M. Zhang, B. Sun, and J. Song, "Effect of inlet and outlet manifolds on regenerative cooling in LOX/methane thrust chambers," *Journal of Thermal Science*, vol. 30, no. 2, pp. 517–529, 2020.
- [23] Y. Zhang, N. Yu, H. Tian, W. Li, and H. Feng, "Experimental and numerical investigations on flow field characteristics of

- pintle injector,” *Aerospace Science and Technology*, vol. 103, p. 105924, 2020.
- [24] N. Zong and V. Yang, “Near-field flow and flame dynamics of LOX/methane shear-coaxial injector under supercritical conditions,” *Proceedings of the Combustion Institute*, vol. 31, no. 2, pp. 2309–2317, 2007.
- [25] H. Huo and V. Yang, “Supercritical LOX/methane combustion of a shear coaxial injector,” in *49th AIAA Aerospace Sciences Meeting including the New Horizons Forum and Aerospace Exposition*, 2011.
- [26] Y. Tian, J. Sun, D. Li, and H. Liu, “An experimental study of LOX/methane subscale injector,” in *Proc. Int. Astronaut. Congr. IAC*, International Astronautical Federation, Toronto, Canada, 2014.
- [27] R. Temam, *Navier-Stokes Equations, Theory and Numerical Analysis*, North-Holland Pub. Co, 1984.
- [28] M. Sellam and A. Chpoun, “Numerical simulation of reactive flows in overexpanded supersonic nozzle with film cooling,” *International Journal of Aerospace Engineering*, vol. 2015, 15 pages, 2015.
- [29] J. L. Hou, P. Jin, and G. B. Cai, “Reduced mechanism for oxygen/methane combustion based sensitivity analysis,” *Journal of Aerospace Power*, vol. 27, no. 7, pp. 1549–1554, 2012.
- [30] B. Magnussen, “On the structure of turbulence and a generalized eddy dissipation concept for chemical reaction in turbulent flow,” in *19th Aerospace Sciences Meeting*, p. 42, 1981.
- [31] I. R. Gran and B. F. Magnussen, “A numerical study of a bluff-body stabilized diffusion flame. Part 2. Influence of combustion modeling and finite-rate chemistry,” *Combustion Science and Technology*, vol. 119, no. 1-6, pp. 191–217, 1996.
- [32] S. B. Pope, “Computationally efficient implementation of combustion chemistry using in situ adaptive tabulation,” *Combustion Theory and Modelling*, vol. 1, no. 1, pp. 41–63, 1997.
- [33] G. Soave, “Equilibrium constants from a modified Redlich-Kwong equation of state,” *Chemical Engineering Science*, vol. 27, no. 6, pp. 1197–1203, 1972.
- [34] R. C. Reid, J. M. Prausnitz, and T. K. Sherwood, *The Properties of Gases and Liquids*, McGraw-Hill, Third edition, 1977.
- [35] T. C. Horng, M. Ajlan, L. L. Lee, K. E. Starling, and M. Ajlan, “Generalized multiparameter correlation for nonpolar and polar fluid transport properties,” *Industrial and Engineering Chemistry Research*, vol. 27, no. 4, pp. 671–679, 1988.
- [36] R. Reitz, “Modeling atomization processes in high-pressure vaporizing sprays,” *Atomisation and Spray Technology*, vol. 3, pp. 309–337, 1987.
- [37] A. B. Liu, D. Mather, and R. D. Reitz, “Modeling the effects of drop drag and breakup on fuel sprays,” *SAE Transactions*, vol. 102, pp. 83–95, 1993.
- [38] J. Locke, S. Pal, and R. Woodward, “Chamber wall heat flux measurements for a LOX/CH₄ propellant uni-element rocket,” in *43rd AIAA/ASME/SAE/ASEE Joint Propulsion Conference & Exhibit*, 2007.
- [39] N. N. Smirnov, V. B. Betelin, V. F. Nikitin, L. I. Stamov, and D. I. Altoukhov, “Accumulation of errors in numerical simulations of chemically reacting gas dynamics,” *Acta Astronautica*, vol. 117, pp. 338–355, 2015.
- [40] N. N. Smirnov, V. B. Betelin, R. M. Shagaliev et al., “Hydrogen fuel rocket engines simulation using LOGOS code,” *International Journal of Hydrogen Energy*, vol. 39, no. 20, pp. 10748–10756, 2014.
- [41] K. Radhakrishnan, S. Min, K. Lee, and J. Koo, “Lagrangian approach to axisymmetric spray simulation of pintle injector for liquid rocket engines,” *Atomization and Sprays*, vol. 28, no. 5, pp. 443–458, 2018.
- [42] J. Tsohas and S. D. Heister, “Numerical simulations of liquid rocket coaxial injector hydrodynamics,” *Journal of Propulsion and Power*, vol. 27, no. 4, pp. 793–810, 2011.